lajss.org
Latin American Journal of Solids and Structures
www.lajss.org

Shock Response of Projectile-Borne Electronics During Concrete Penetration: Theoretical Modeling and Numerical Simulation

Qiang Sheng [a] 0009-0009-6457-7320, Xiaoye Bie [a] 0009-0001-0873-3351, Changsheng Li [a*] 0000-0003-2451-7680, He Zhang [a] 0000-0002-3803-8149

[a] School of Mechanical Engineering, Nanjing University of Science and Technology, Nanjing 210094, China. Email:3581368151@qq.com, lcsnjust@njust.edu.cn, 224101030109@ njust.edu.cn, hezhangz@mail.njust.edu.cn

* Corresponding author

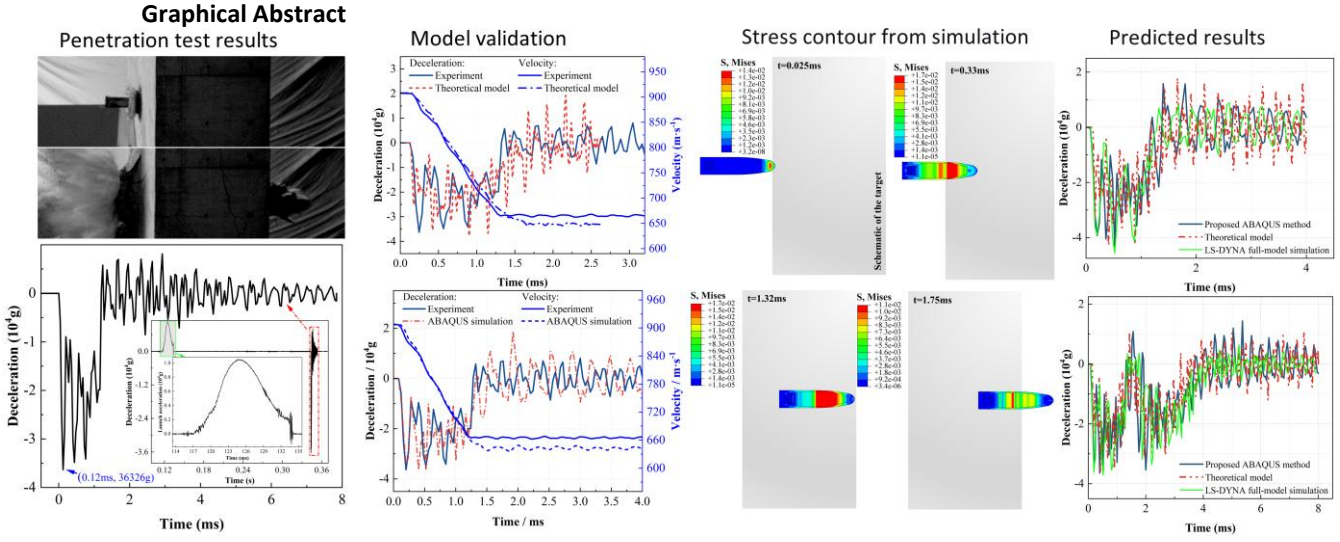
Abstract

Predicting the shock response of projectile-borne electronics under high-velocity concrete penetration is a key challenge in impact dynamics. This study developed a dynamic model integrating stress wave propagation, nonlinear mechanical behavior of cushion materials, and nonlinear interfacial contact between internal components. The model was compared against a single ballistic impact test at 908 m/s and exhibited good agreement with the measured deceleration history. An efficient ABAQUS/Explicit simulation with a user-defined load subroutine was developed to avoid explicit target modeling. This approach produced a peak deceleration difference of 0.25% relative to experimental data, with pulse width and residual velocity deviations of 9.1% and 3.3%, respectively. In cross-comparisons with LS-DYNA full-model simulations, both methods yielded Pearson correlation coefficients ranging from 0.89 to 0.96 for projectile responses and from 0.70 to 0.83 for electronic modules under various impact conditions. Parametric analyses indicated that the shock amplification factor from the projectile body to the electronic module increased from 1.28 to 1.54 as the impact velocity increased from 600 m/s to 1000 m/s. Increasing the CRH from 1 to 3 reduced the peak deceleration of the electronic module by approximately 12,000 g. For successive double impacts, a sufficiently long interval weakens the influence of the first impact on the second-impact response. These findings provide a theoretical basis and technical support for the shock-resistant design of the onboard electronics in high-overload environments.

Keywords

Dynamic response, penetration overload, stress-wave propagation, projectile-borne electronics, numerical simulation

Graphical Abstract



1 INTRODUCTION

Kinetic projectile penetration of concrete fortifications and planetary lander touchdown on extraterrestrial surfaces represent typical high-velocity impact scenarios in aerospace engineering. In such events, the intense interaction between a projectile or lander and its target directly threatens the survival of projectile-borne electronics. Taking the example of a kinetic projectile penetrating concrete, the projectile endures a transient impact with peak accelerations reaching hundreds of thousands of times Earth's gravitational acceleration within a few milliseconds (Cao et al., 2026; Mercurio et al., 2025; Feng et al., 2018; Glößner et al., 2017). The internal electronics must maintain both structural integrity and functional performance under such extreme mechanical conditions. Therefore, accurately predicting the dynamic responses of projectile-borne electronics throughout the high-velocity impact process has become a key scientific challenge for improving their survivability and operational reliability (Verberne et al., 2026).

Penetration overload directly reflects the dynamic environment of the projectile and serves as a key basis for analyzing the dynamic response of projectile-borne electronics. Experimental measurements have shown that these overload signals possess high amplitudes and a broad frequency bandwidth (Fu et al., 2022; Warren et al., 2014; Booker et al., 2009; Wu et al., 2015; Peng et al., 2019). Most theoretical studies adopted the rigid-body assumption and focused on projectile overload responses (Chen et al., 2014; Ben-Dor et al., 2007; Guo et al., 2023; Yankelevsky, 2017; Esaker et al., 2023). In practice, the impact load varies in amplitude when propagating through the projectile structure and connection interfaces. This creates substantial discrepancies between the overloads acting on the electronic modules and those on the projectile body. Thus, projectile overload cannot be directly used as the design input for shock-resistant optimization of electronic modules. The dynamic responses of projectile-borne electronics have been mainly investigated via numerical simulations (Yang et al., 2026; Chakka et al., 2008; Zhang et al., 2023). While these high-fidelity simulations compensate for the limitations of traditional rigid-body dynamics models in capturing high-frequency dynamic characteristics, they suffer from excessive computational consumption. Some researchers have developed simplified theoretical models to explore the influence of threaded connections on the dynamic characteristics of the electronics (Zhang et al., 2017; Zhang et al., 2016; Yan et al., 2021). Beyond structural connections, several studies have further investigated the dynamic response of the projectile and its internal electronics. Cheng et al. (2020) found that the projectile exhibited characteristics of vibration amplification and periodic oscillation, which are also the primary factors affecting the response characteristics of the circuit module. Yu et al. (2023) developed a viscoelastic model to predict the dynamic responses of the projectile-borne electronics. However, these prior studies neglected the stress wave propagation effects during impact and thus failed to capture the high-frequency vibration response of the system.

To overcome the limitations of the traditional rigid-body and linear assumptions, this study developed a dynamic overload calculation model that integrates stress wave propagation and nonlinear interfacial contacts between components, enabling accurate prediction of overloads on projectile-borne electronics. Furthermore, an efficient ABAQUS/Explicit-based simulation approach was developed, in which projectile–target interaction was modeled via a user-defined load subroutine. This method eliminated the need for target modeling, significantly improving computational efficiency. Subsequently, the effects of factors such as impact velocity and the caliber-radius-head (CRH) ratio on overloads were analyzed. The proposed model and efficient simulation approach offer valuable guidance for the shock-resistant design of projectile-borne electronics.

2 SHOCK RESPONSE MODEL OF PROJECTILE-BORNE ELECTRONICS

2.1 Structural vibration model of the projectile

During the penetration process, the projectile is subjected to a time-varying resistive force. The normal stress σ_n acting on the projectile can be expressed as (Warren and Forquin, 2016; Warren and Hanchak, 2004):

$$\sigma_n = R + \rho_t \cdot {v_n}^2 = R + \rho_t \cdot (v \cdot cos\,\theta)^2 \tag{1}$$

where ρ_t denotes the concrete density; R represents the static resistance; v denotes the axial velocity of the projectile; and θ represents the angle between the normal vector of a differential surface segment on the projectile surface and the projectile axis.

The geometric parameterization of the projectile contour in the local coordinate system is expressed as:

$$P(x, \Phi) = [x, r(x)\,cos\,\Phi\,, r(x)\,sin\,\Phi] \tag{2}$$

where x is the axial coordinate; Φ is the circumferential polar angle, satisfying $\Phi \in [0, 2\pi]$; and $r(x)$ is the cross-sectional radius of the projectile at axial position x. For a parameterized surface $P(x, \Phi)$, its normal vector is given by:

$$\boldsymbol{n} = \frac{\partial P}{\partial x} \times \frac{\partial P}{\partial \Phi} = \begin{vmatrix} i & j & k \\ 1 & k_r \cos\Phi & k_r \sin\Phi \\ 0 & -r\sin\Phi & r\cos\Phi \end{vmatrix} \quad , \quad k_r = \frac{dr}{dx} \tag{3}$$

Thus, the normal angle θ at any axial position along the projectile can be determined by:

$$\theta = \begin{cases} arctan(1/k_r) & , \quad k_r \geq 0 \\ \pi + arctan(1/k_r) \, , k_r < 0 \end{cases} \tag{4}$$

The frictional force acting on the projectile surface is given by (Fu et al., 2022):

$$\sigma_t = \mu \cdot \sigma_n \tag{5}$$

where μ is the friction coefficient.

The analytical formulation for the radial stress applicable to finite-thickness concrete targets is given as follows (Warren and Hanchak, 2004):

$$\sigma_r(a) = \Bigg\{ 2\rho_t \dot{a} \left[\frac{1}{\alpha\lambda - 4} - \frac{1}{\alpha\lambda - 1} \right] - \frac{\tau}{\lambda} + \left(\frac{2E_t}{3\tau} \right)^{\frac{\alpha\lambda}{3}} \left\{ \frac{2\tau}{3} \left[1 - \left(\frac{b}{d_t} \right)^3 \right] + 2\rho_t \dot{a} \left[\frac{\alpha\lambda}{\alpha\lambda - 1} \cdot \left(\frac{3\tau}{2E_t} \right)^{\frac{1}{3}} \right. \right. \tag{6}$$

$$\left. \left. - \frac{1}{4} \frac{\alpha\lambda}{\alpha\lambda - 4} \left(\frac{3\tau}{2E_t} \right)^{\frac{4}{3}} - \frac{a}{d_t} + \frac{1}{4} \left(\frac{a}{d_t} \right)^4 \right] + \frac{\tau}{\lambda} \right\} \Bigg\}, \quad d_t \geq b$$

where a represents the cavity radius; $\dot{a}$ is the cavity expansion velocity; E_t represents the elastic modulus of the concrete; $\alpha = 6/(3 + 2\lambda)$ is an intermediate variable; τ and λ denote the cohesive strength and pressure hardening coefficient of the concrete, respectively; b represents the radial length at the interface between the plastic zone and elastic zone; and d_t is defined as the sum of the cavity radius a and the distance from the outward normal of the differential segment to the free surface. The function of free-surface effect takes the form (Warren and Hanchak, 2004):

$$f(d_t, a, \dot{a}) = \begin{cases} \dfrac{\sigma_r(a)}{\sigma_r(a)_{d\to\infty}}, d_t \geq b \\ 0, d_t < b \end{cases} \tag{7}$$

Thus, the axial resistance acting on the projectile can be written as:

$$df_x = \sigma_n(\cos\theta + \mu \sin\theta) \cdot f(d_t, a, \dot{a}) ds \tag{8}$$

To establish the vibration model for the projectile, the following assumptions are adopted: (1) during penetration, only axial stress wave propagation within the projectile is considered, while transverse deformation and rotational effects are neglected; (2) projectile–target interaction is represented by an axial load acting on the projectile surface; and (3) the feedback effects of target deformation and failure on projectile motion are neglected. The projectile is idealized as a one-dimensional rod with diameter d, length l and cross-sectional area $A = A(x)$. The projectile is assigned an initial velocity along the x-axis.

According to D'Alembert's principle, the equation of motion for a differential segment of length dx located at position x along the projectile is expressed as:

$$\sigma(x+dx,t)\cdot A(x+dx)-\sigma(x,t)\cdot A(x)+f(x,t)dx=\rho A(x)dx\frac{\partial^2 u(x,t)}{\partial t^2} \tag{9}$$

where ρ is the material density; $f(x,t)$ is the rigid-body resistance experienced per unit length of a differential segment; $A(x)$ is the cross-sectional area of the projectile at axial position x; $\sigma(x,t)$ is the axial stress at position x and time t.

By applying a Taylor series expansion, Eq. (9) is transformed into:

$$\sigma(x,t)\frac{\partial A(x)}{\partial x}+A(x)\frac{\partial \sigma(x,t)}{\partial x}+f(x,t)=\rho A(x)\frac{\partial^2 u(x,t)}{\partial t^2} \tag{10}$$

During stress wave propagation, the stress state depends on strain and strain-rate. Considering the complexity of the projectile's plastic constitutive behavior, a bilinear elastoplastic model is adopted for analytical tractability, formulated as follows:

$$\sigma_y=\begin{cases}E\varepsilon \quad , \quad \sigma_y\le\sigma_0\\ \sigma_0+E_t\varepsilon^p, \sigma_y>\sigma_0\end{cases} \tag{11}$$

where σ_0 is the initial yield stress; E is the elastic modulus; E_t is the plastic hardening modulus; ε and ε^p are the plastic strain.

The projectile impacts the concrete target at an initial velocity of V_0. The initial conditions for the projectile are listed in Eq. (12).

$$u(x,0)=0 \quad , \quad \frac{\partial u(x,0)}{\partial t}=V_0 \quad , \quad \sigma(x,0)=0 \tag{12}$$

Prior to exiting the target, the projectile nose experiences resistance and remains in a constrained state. Conversely, after the projectile exits the target, the nose transitions to a free boundary condition. The boundary conditions are listed in Eqs. (13) and (14).

$$\begin{cases}\sigma(0,t)\cdot A(0)=f(0,t)\\ \sigma(l,t)\cdot A(l)=0\end{cases} \tag{13}$$

where $f(0,t)$ is the resistance experienced per unit length of the differential segment at the projectile tip at time t; $A(0)$ and $A(l)$ are the cross-sectional areas at the projectile tip and afterbody, respectively.

$$\begin{cases}\sigma(0,t)\cdot A(0)=0\\ \sigma(l,t)\cdot A(l)=0\end{cases} \tag{14}$$

Eq. (10) takes the form of a nonlinear partial differential equation that does not admit an explicit analytical solution. The finite difference method is adopted to discretize the equation into a system of algebraic equations at discrete nodal points. This enables iterative computations to sequentially resolve the displacement, stress, and other key responses at each discrete element of the projectile.

The projectile is discretized axially into n discrete segments, each of length $\Delta x = l/n$. Spatial nodes are assigned indices $i=0,1,2,\dots,n$, with positions given by $x_i=i\cdot\Delta x$. The time domain $[0,T]$ is divided into m uniform time steps of duration $\Delta t = T/m$, and temporal nodes are indexed by $j=0,1,2,\dots,m$, where the discrete time instants are defined as $t_j=j\cdot\Delta t$.

The term $u_{i,j}=(x_i,t_j)$ represents the approximate displacement of the projectile at position x_i and time t_j. Strain is the first-order derivative of displacement with respect to space, denoted as $\varepsilon(x,t)=\frac{\partial u(x,t)}{\partial x}$. According to the central difference approximation, $\varepsilon(x,t)$ at node (x_i,t_j) can be approximated as:

$$\varepsilon_{i,j}=\frac{u_{i+1,j}-u_{i-1,j}}{2\Delta x} \tag{15}$$

Based on the Taylor series expansion and the central difference approximation, the partial derivatives in Eq. (10) are discretized at node (x_i, t_j) and expressed as:

$$\frac{\partial^2 u(x,t)}{\partial t^2} = \frac{u_{i,j+1} - 2u_{i,j} + u_{i,j-1}}{\Delta t^2} \tag{16}$$

$$\frac{\partial \sigma(x,t)}{\partial x} = \frac{\sigma_{i+1,j} - \sigma_{i-1,j}}{2\Delta x} \tag{17}$$

$$\frac{\partial A(x)}{\partial x} = \frac{A_{i+1} - A_{i-1}}{2\Delta x} \tag{18}$$

Substituting Eqs. (16) through (18) into Eq. (10) yields the discrete equation of motion for a differential segment:

$$u_{i,j+1} = 2u_{i,j} - u_{i,j-1} + \frac{\Delta t^2}{2\rho A_i \Delta x}\left(A_i\left(\sigma_{i+1,j} - \sigma_{i-1,j}\right) + \sigma_{i,j}(A_{i+1} - A_{i-1})\right) + \frac{\Delta t^2}{\rho A_i} \cdot f(x_i, t_j) \tag{19}$$

With $u_{i,0} = 0$ and $u_{i,1} = \Delta t V_0$ from forward differencing, the stresses are obtained via the constitutive model, allowing iterative calculation of $u_{i,j+1}$ for further steps.

2.2 Dynamic overload model of projectile-borne electronics

The projectile consists mainly of the base plug, electronics, buffers, and ancillary components. The base plug is threaded onto the projectile. The electronics comprise a mechanical housing, polyurethane, a circuit board, and a high-g sensor (Figure 1). Due to their relatively small mass, the PCB and sensor are considered as a single electronic module for analysis.

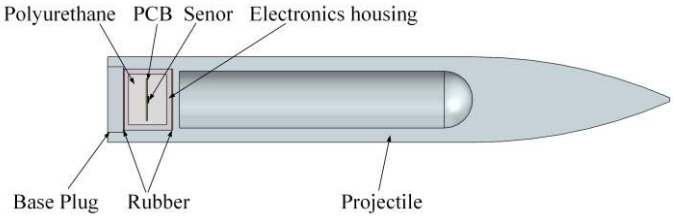


Figure 1 Schematic diagram of the projectile.

The load on the projectile is transmitted to the electronics housing through the rubber cushions and the threaded connection, and then to the electrical module via the potting compound. Applying D'Alembert's principle, the dynamic overload model for the onboard electronics is governed by the following expressions:

$$\begin{cases} m_b \ddot{x}_b = -F_{h1} - F_s \\ m_f \ddot{x}_f = F_g + F_{h1} - F_{h2} \\ m_e \ddot{x}_e = -F_g \\ F_{h1} = 0 \quad , \quad x_f > x_{wf} \\ F_{h2} = 0 \quad , \quad x_f \le x_{wf} \end{cases} \tag{20}$$

where m_w, m_b, m_f, and m_e represent the equivalent masses of the projectile, base plug, electronics housing, and electrical module, respectively; $x_{wb}(t)$ and $x_{wf}(t)$ represent the displacement responses at the mounting locations of the base plug and electronics on the projectile aft section, obtained from Equation(19); $x_b(t)$, $x_f(t)$, and $x_e(t)$ represent the absolute displacements of the base plug, electronics housing, and electrical module, respectively. Their second-order time derivatives yield the corresponding overload responses. F_s denotes the equivalent force generated by the threaded connection; F_{hi} and F_g denote the equivalent response forces resulting from the deformation of the rubber and polyurethane, respectively. Since the rubber at both ends of the electronics housing cannot be compressed simultaneously, the force acting on it depends on the relative displacement between x_f and x_{wf}.

2.2.1 Equivalent force of threaded connection

Since the thread teeth possess a much smaller mass compared with the bolt and nut, their inertial effects can be neglected under dynamic loading, and they essentially behave as stiffness elements (Zhang and Gao, 2022). To address the interfacial mechanics, a calculation model was developed (Lu et al., 2019) for axial force distribution and stiffness that includes frictional factors at threaded connections. This model gives the equivalent stiffness of the threaded engagement portion as:

$$k_c = \frac{1}{n(\delta_b + \delta_n) \cdot sin\,\eta} \cdot \frac{cosh(zl_s) - 1}{sinh(zl_s)} \tag{21}$$

where δ_b and δ_n are the total deformations of the bolt and nut, per unit width under a unit axial load; η is the thread lead angle; z is a comprehensive coefficient accounting for material properties, cross-sectional parameters, and local deformation effects; and l_s is the length of the threaded connection. The equivalent response force of the threaded connection is expressed as:

$$F_s = k_c x_s \tag{22}$$

2.2.2 Equivalent force of rubber deformation

Rubber is a hyperelastic material that exhibits a nonlinear stress-strain relationship. Its mechanical behavior can be characterized using the Mooney–Rivlin model (Khajehsaeid et al., 2013; Mooney, 1940):

$$W = \sum_{i+j=1}^{n} C_{ij}\,(I_1 - 3)^i (I_2 - 3)^j \tag{23}$$

where C_{ij} is a material constant related to the deformation response, I_1 and I_2 is the strain invariant.

The mechanical behavior of viscoelastic materials is typically described using the Wiechert model (Machiraju et al., 2006):

$$\sigma(\varepsilon, t) = \sigma_E(\varepsilon) \cdot g(t) = \sigma_E(\varepsilon)\left(g_\infty + \sum_{i=1}^{N} g_i \cdot exp(-\beta_i t)\right) \tag{24}$$

where $\sigma\,(\varepsilon, t)$ represents the stress under strain ε and at time t; σ_E is the engineering stress; the time-dependent function $g\,(t)$ is expressed via a Prony series; β_i is the reciprocal of the relaxation time; and g_∞ and g_i are dimensionless constants satisfying the normalization condition $g_\infty + \sum_{i=1}^{N} g_i = 1$. When $t = 0, g(0) = 1$,and $\sigma(\varepsilon, 0) = \sigma_0(\varepsilon)$. The term $g(\infty) = g_\infty$ represents the stress-strain relationship in the long-term or equilibrium state, where $\sigma(\varepsilon, \infty) = g_\infty \cdot \sigma_0(\varepsilon)$.

Ramp-loading tests are currently employed to investigate the stress–strain behavior of rubber materials at various displacement rates. The time-dependent stress response under ramp loading was computed using the following convolution integral (Chen et al., 2022):

$$\sigma(\varepsilon, t) = g_\infty \sigma_E(\varepsilon) + \sum_{i=1}^{N} g_i \int_0^t exp(-\beta_i(t - s)) \frac{d\sigma_E(\varepsilon)}{ds} ds \tag{25}$$

A mathematical characterization model for the nonlinear resilience of rubber is constructed as follows:

$$F_h(x_r, t) = g_\infty F_0(x_r) + \sum_{i=1}^{N} g_i \int_0^t exp(-\beta_i(t - s)) \frac{\partial F_0(x_r)}{\partial s} ds \tag{26}$$

where x_r is the compressive deformation of the rubber.

2.2.3 Equivalent force of polyurethane deformation

A low-parameter, semi-empirical constitutive equation is established to characterize the nonlinear mechanical behavior of porous materials such as foams during compression (Jeong et al., 2012):

$$\sigma_p(\varepsilon) = k_1\left(1 - exp\left(-\frac{k_2}{k_1}\varepsilon(1-\varepsilon)^{k_3}\right)\right) + k_4\left(\frac{\varepsilon}{1-\varepsilon}\right)^{k_5} \tag{27}$$

where σ_p and ε represent the nominal stress and nominal strain, respectively; k_1, k_2 and k_4 represent density-dependent parameters, where k_1 denotes the plateau stress; k_2 denotes the elastic modulus of the material in the elastic stage; and k_3 and k_5 are empirical coefficients reflecting the material properties.

Since the original Avalle model does not account for strain-rate effects, strain-rate-dependent parameters are introduced to modify the model accordingly.

$$M(\varepsilon, \dot{\varepsilon}) = 1 + (k_6 + k_7\varepsilon)\left(1 + k_8\, ln\left(\frac{\dot{\varepsilon}}{\dot{\varepsilon}_0}\right)\right) \tag{28}$$

where $M(\varepsilon, \dot{\varepsilon})$ is a function of strain and strain rate; $\dot{\varepsilon}_0$ represents the reference strain rate; k_6, k_7, and k_8 are parameters to be fitted.

Then, its instantaneous response force is expressed as:

$$F_g = \left[k_1\left(1 - exp\left(-\frac{k_2}{k_1}\left(1 - \frac{x_p}{L_p}\right)^{k_3}\frac{x_p}{L_p}\right)\right) + k_4\left(\frac{x_p}{L_p - x_p}\right)^{k_5}\right] \cdot \left[1 + \left(k_6 + \frac{k_7 x_p}{L_p}\right)\left(1 + k_8\, ln\left(\frac{\dot{x}_p}{L_p\dot{\varepsilon}_0}\right)\right)\right] S_0 \tag{29}$$

where L_p is the initial length of the polyurethane, S_0 is the cross-sectional area, and x_p is the deformation under compressive loading.

By substituting Eqs. (22), (26), and (29) into Eq. (20), we obtain the overload expression of the projectile-borne electronics.

3 EXPERIMENTAL SETUP AND MODEL COMPARISON

3.1 Impact test

3.1.1 Test setup

The projectile used in this study had a total length of 665 mm and a diameter of 155 mm. It was fabricated from 30CrMnSiNi2A steel, as was its base plug. The total mass of the projectile was 42.9 kg, of which the base plug accounted for 4.69 kg, the electronics housing for 0.36 kg, and the PCB and sensor for 0.075 kg. The electronics housing was filled with polyurethane. The stiffness coefficient k_c of the threaded connection is 9.48 × 10^9 N/m. Figure 2 depicts the projectile and the experimental setup.

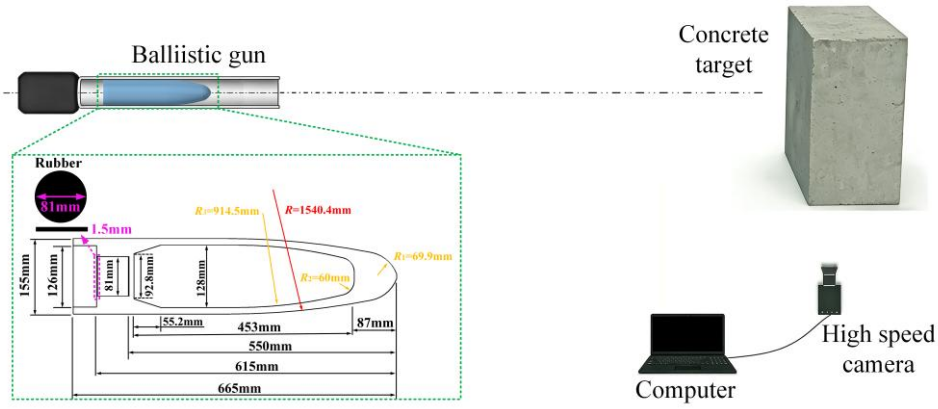


Figure 2 Schematic diagram of the experimental setup.

The experimental setup comprised a ballistic gun, a projectile, a concrete target, and a high-speed imaging system. The concrete target had a thickness of 1 m and a compressive strength of 40 MPa. The initial velocity of the projectile was obtained as 908 m/s by integrating the acceleration signal during the launch stage.

3.1.2 Experimental results and analysis

As shown in the high-speed camera images of Figure 3, the projectile impacted the target vertically. Upon initial impact, the front surface of the target fragmented under intense shock loading, ejecting concrete debris and forming a front crater. During penetration, the projectile was fully engulfed by the target, the dust cloud continued to expand, and radial compression drove the formation of macroscopic lateral cracks in the target. Stress wave reflection induced tensile spalling on the rear face of the target. From the high-speed camera images, the impact velocity and residual velocity were measured as 915 m/s and 667 m/s, respectively.

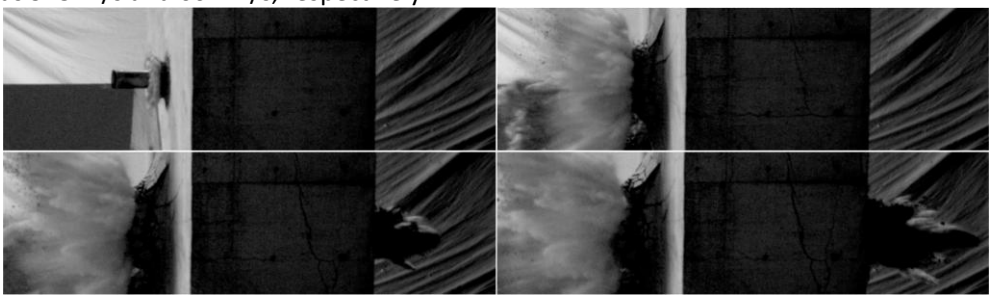


Figure 3 High-speed camera images of the projectile penetration process.

Acceleration was measured using a miniature high-g accelerometer (dimensions: 10 mm × 15 mm × 5 mm; range: 70,000 g; sensitivity: 0.5 μV/g). The accelerometer was mounted on the circuit board, and the board was potted in the electronics housing. The signal was recorded by the onboard data acquisition system at a sampling frequency of 25 kHz. Figure 4 depicts the raw acceleration signal captured by the electrical module, covering both the launch and penetration stages. The maximum axial acceleration reached 36,326 g. After approximately 1.3 ms of penetration, the projectile nose exited the target, resulting in a rapid attenuation of the acceleration. The residual velocity after perforation was 664 $m \cdot s^{-1}$, which was obtained by integrating the measured acceleration–time curve. The velocities derived by integrating the measured acceleration signal agreed with high-speed camera recordings to within 1%, confirming the reliability of the acceleration data. The initial impact velocity of 908 m/s obtained from acceleration integration was adopted in the subsequent analysis.

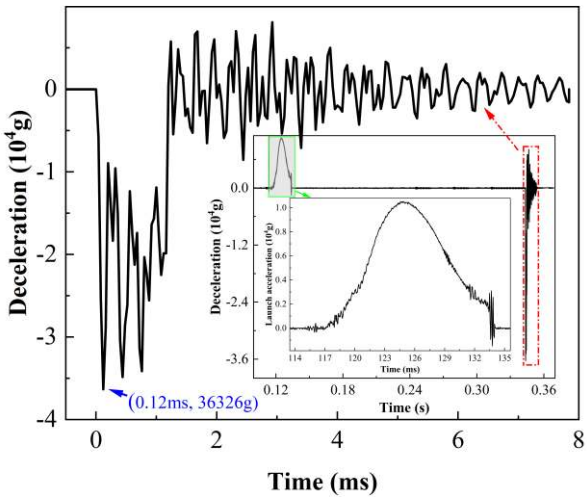


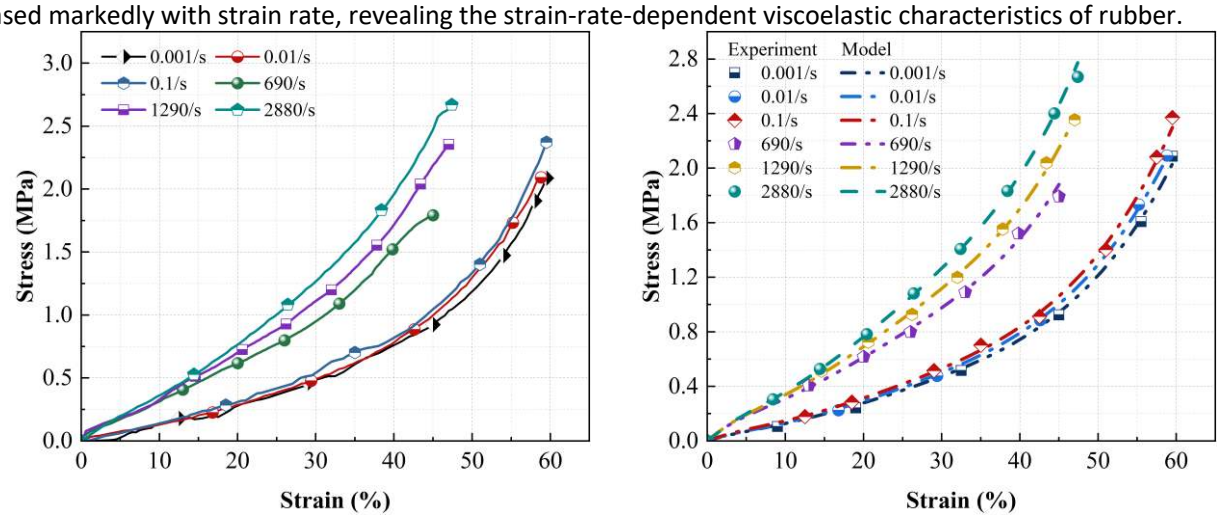
Figure 4 The raw deceleration-time history curve obtained from the experiment.

3.2 Mechanical property tests and determination of material parameters

Uniaxial compression tests were performed on rubber and polyurethane specimens using a universal testing machine for quasi-static loading and a split Hopkinson pressure bar (SHPB) for dynamic loading. All tests were conducted at room temperature. The specimens for quasi-static compression were Φ10 mm × 10 mm cylinders, while those for SHPB dynamic tests were Φ10 mm × 5 mm cylinders. Each test condition was repeated at least three times, and the averaged stress–strain responses were used for subsequent analysis.

3.2.1 Cushioning rubber parameters

To overcome the impedance mismatch between the low-wave-impedance rubber and conventional steel bars, aluminum alloy incident and transmission bars were employed in the SHPB setup. A pulse-shaping technique was also applied to facilitate early stress equilibrium and mitigate dispersion effects. Figure 5 presents the stress–strain curves of the rubber over strain rates ranging from 0.001 s^{-1} to 1880 s^{-1}. The results showed that at identical strain levels, stress increased markedly with strain rate, revealing the strain-rate-dependent viscoelastic characteristics of rubber.



(a) (b)

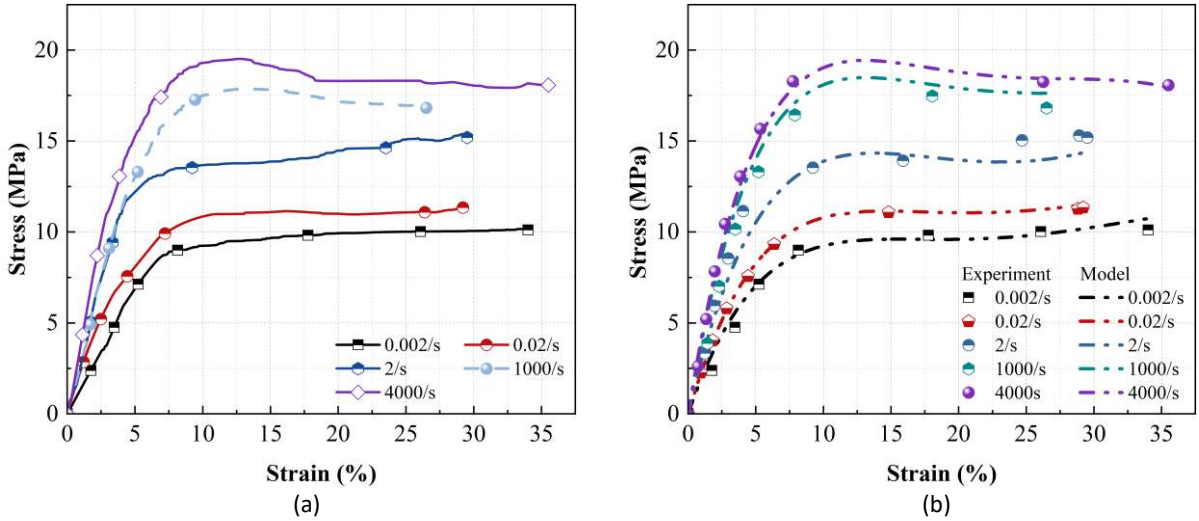
Figure 5 Stress-strain curves of the cushioning rubber: (a) experimental curves, and (b) parameter-fitted curves.

A three-term Prony series (N = 3) was fitted to the experimental data, yielding a coefficient of determination (R^2) ranging from 0.997 to 0.999 and mean relative errors (MRE) between 0.53% and 6.32%, indicating good agreement between the model predictions and experimental data. The fitted parameters are listed in Table 1.

Table 1 Identified material parameters for the cushioning rubber.

Mooney-Rivlin Parameter (MPa)						
C_{10}	C_{01}	C_{20}	C_{11}	C_{02}		
-5.667	6.582	41.336	-110.374	78.974		
Prony series Parameter (β: s^{-1})						
g_1	g_2	g_3	g_∞	β_1	β_2	β_3
0.051	0.094	0.559	0.296	0.004	1.859	5661.683

3.2.2 Polyurethane material parameters



(a) (b)

Figure 6 Stress-strain curves of the polyurethane: (a) experimental curves, and (b) parameter-fitted curves.

Figure 6 presents the compressive stress–strain responses of polyurethane at strain rates ranging from quasi-static (2×10^{-3} s^{-1}) to dynamic (4×10^{3} s^{-1}), showing a pronounced strain-rate dependence. The identified parameters for the polyurethane constitutive model are summarised in Table 2, with a reference strain rate of 0.002 s^{-1}. The model predictions agreed well with the experimental data across all five strain-rate conditions, with R^2 values ranging from 0.956 to 0.999 and MRE from 1.92% to 14.4%. The maximum error of 14.4% occurred at an intermediate strain rate of 2 s^{-1}.

Table 2 Fitting results for the constitutive model parameters of polyurethane.

Parameter	k_1	k_2	k_3	k_4	k_5	k_6	k_7	k_8
Value	33295.064	49.85	8.937	12.799	1.32	3.168	-6.757	0.102

3.3 Comparison of the theoretical model with the experiment

As described in Section 2.1, the projectile is idealized as a one-dimensional rod. The internal components of the projectile have a total mass of only 0.435 kg, accounting for approximately 1% of the overall projectile mass (42.9 kg). Accordingly, these components are neglected in the one-dimensional theoretical model, and only the projectile body and the base plug are considered. The cross-sectional area $A(x)$ is determined from the actual geometric profile of the projectile. The piecewise expression for $A(x)$ is given by Eq. (30). In the numerical solution, the discontinuities in $A(x)$ are treated as internal interfaces, where the continuity conditions of displacement and axial force are enforced.

$$A(x)=\begin{cases}\pi\left[-19.6379+\sqrt{(69.87^2-(x+65.38)^2)}\right]^2, x\in[-52,0]\\ \pi\left[-1462.971+\sqrt{1540.421^2-(x+347)^2}\right]^2, x\in[-87,-52]\\ \pi\left\{\left[-1462.971+\sqrt{1540.421^2-(x+347)^2}\right]^2-\left[8.758+\sqrt{900-(x+117)^2}\right]^2\right\}, x\in[-109.88,-87]\\ \pi\left\{\left[-1462.971+\sqrt{1540.421^2-(x+347)^2}\right]^2-\left[-850.5+\sqrt{914.5^2-(x+326.8)^2}\right]^2\right\}, x\in[-326.8,-109.88]\\ \pi\left\{\left[-1462.971+\sqrt{1540.421^2-(x+347)^2}\right]^2-64^2\right\}, x\in[-347,-326.8]\\ 1902.5025\pi, x\in[-484.8,-347]\\ \pi[77.45^2-(0.31884x+218.574)^2], x\in[-540,-484.8]\\ 5998.5025\pi, x\in[-550,-540]\\ 4358.2525\pi, x\in[-616.8,-550]\\ 5998.5025\pi, x\in[-665,-616.8]\end{cases} \tag{30}$$

The concrete material parameters adopted in the numerical model are listed in Table 3. The Courant–Friedrichs–Lewy (CFL) stability criterion was followed in this study. Considering the abrupt cross-sectional variations of the projectile, the computational domain was discretized in a piecewise non-uniform scheme. Each segment was uniformly meshed with a target nodal spacing of 3.0 mm. This meshing strategy yielded a minimum nodal spacing of 3.0 mm across the computational domain. Based on the fixed time step of $\Delta t = 0.5\ \mu s$ and a longitudinal wave speed of $c = 5135$ m/s, the maximum CFL number was calculated to be approximately 0.86. This value was below unity, satisfying the stability requirement for the explicit solution scheme. A discretization-sensitivity analysis indicated that the adopted spatial and temporal discretization parameters ensured reliable numerical convergence for dynamic response prediction. The relative deviation of peak acceleration remained below 4.6% after halving both spatial and temporal step sizes. Based on the integrated results of the measured acceleration signal, an impact velocity of 908 m/s was adopted for the numerical calculations. The rigid-body theoretical model (Eq. (8)) was employed to predict the projectile deceleration. The resulting time-history curve is shown in Figure 7a, with a peak deceleration of approximately 23,930 g. Although this rigid-body-based model accurately predicted the global penetration state, it failed to capture the actual dynamic response characteristics.

Table 3 Material parameters of the concrete (Liu et al., 2025; Zhu et al., 2025).

Parameter	ρ_t / g·cm^{-3}	f_t / MPa	E / GPa	τ / MPa	λ
Value	2.4	40	32.5	31.07	0.67

Table 4 Comparison between theoretical predictions and experimental data.

Data type	Model prediction	Experiment	Error
Peak deceleration / g	37858	36326	4.2%
Pulse width / ms	1.52	1.32	15.2%
Residual velocity / (m· s^{-1})	647	664	2.6%

Figure 7 presents the deceleration curves of the projectile and the electrical module. The propagation of stress waves through the projectile induced structural vibration, resulting in a peak deceleration of 25,687 g. The internal electrical module exhibited more pronounced vibration, with a maximum deceleration of approximately 37,858 g. The theoretical peak deceleration of the module exceeded the measured value by 4.2%; the pulse width error was 15.2%, and the residual velocity error was 2.6%, as summarized in Table 4. The electrical module received base excitation from upstream components. Factors such as interface stiffness and uneven mass distribution amplified its response. The electrical module was subjected to more severe dynamic loads, which necessitated improved shock resistance.

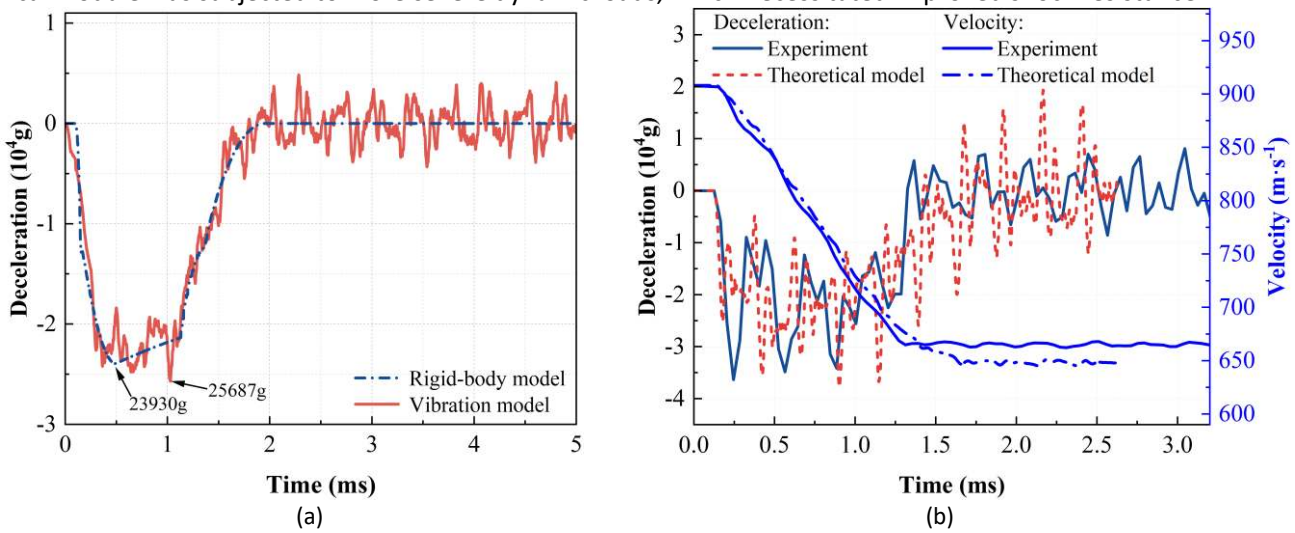


Figure 7 Prediction results: (a) projectile decelerations, and (b) comparison between experiment and theoretical model.

4 DISCUSSION

The primary focus of this study is not on the failure behavior of concrete targets but rather on the dynamic response of projectile-borne electronics under penetration-induced loading. This section presents an efficient numerical simulation approach based on ABAQUS/Explicit to characterize the dynamic response (Figure 8). Based on the projectile-target contact resistance function described in Section 2.1, a user-defined load subroutine was developed and implemented as a boundary condition on the projectile surface. Upon penetration of the projectile into the target at a non-zero velocity, the subroutine calculated the instantaneous normal stress distribution on the projectile surface. The total resistance was obtained by integrating the forces over all micro-elements. The calculation terminated once the projectile velocity decreased to zero or all micro-elements exited the target domain.

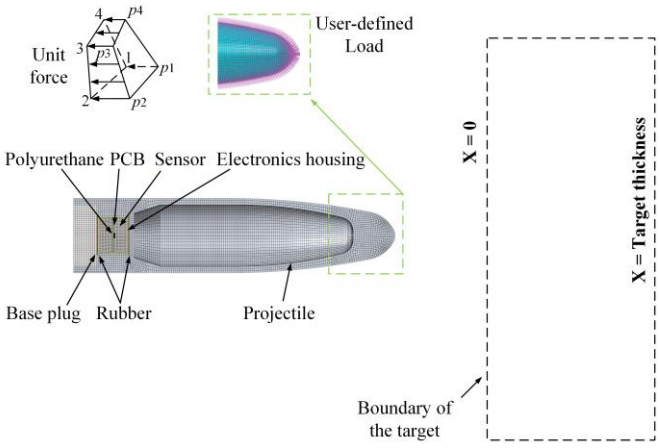


Figure 8 Efficient simulation approach.

To assess the accuracy of this method, a simulation model was established based on the experiment described in Section 3.1. C3D8R solid elements were adopted, with local mesh refinement applied at the projectile nose and tail (element size ≈ 2.0 mm), while a coarser mesh (≈ 4.0 mm) was employed for the remaining regions, yielding a total of 176,824 elements. Material parameters for all components are listed in Table 5. The rubber material was modeled using a second-order hyperelastic polynomial constitutive model combined with a viscoelastic Prony series, whose parameters are summarized in Table 1. The polyurethane was modeled as a rate-dependent low-density foam, with its stress-strain curves at different strain rates (Figure 6) directly imported. The PCB and sensor were modeled as homogeneous epoxy resin, in accordance with Yu et al. (2023), Zhu et al. (2024), and Yang et al. (2026). The base plug–projectile threaded connection was modeled using a tied constraint, a widely adopted simplification in impact dynamics (Yan et al., 2022), while general contact pairs were assigned to all other interfaces. An initial velocity was assigned to the projectile through a predefined field. The ratio of artificial strain energy to total internal energy remained below 1.76% throughout the explicit analysis, demonstrating that artificial strain energy had a negligible effect on the solution. A mesh convergence study was conducted using three mesh discretizations: coarse (106,960 elements, average element size of 3.8 mm), medium (176,824 elements, average element size of 3.2 mm), and fine (726,960 elements, average element size of 2.0 mm). The coarse mesh yielded an overall relative deviation of approximately 5.85% compared with the fine-mesh results. For the medium-density mesh, the relative differences fell below 0.60% for peak acceleration and 0.45% for residual velocity, and the corresponding time-history curves were nearly superimposed. This demonstrated that the selected mesh density was capable of resolving the dynamic response with satisfactory accuracy while balancing computational cost, and all subsequent simulations were carried out using this mesh scheme.

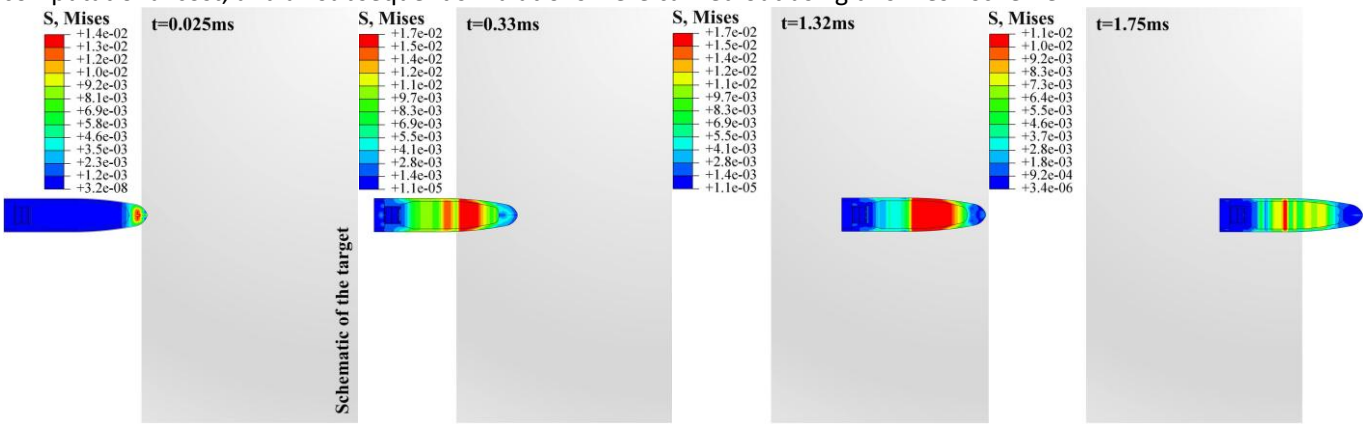


Figure 9 Equivalent stress contours of the projectile at different times.

Table 5 Material parameters of the projectile and its internal components (Peng et al. ,2023; Zhu et al. ,2024).

Component name	Material	Density / g·cm^{-3}	Elastic modulus / GPa	Poisson ratio	Yield strength / MPa	Et / GPa
Projectile	30CrMnSiNi2A	7.8	207	0.30	1720	5
Base plug	30CrMnSiNi2A	7.8	207	0.30	1720	5
Electronics housing	Aluminum alloy	2.7	70.1	0.33	430	2.3
Sensor	Epoxy resin	1.97	26	0.30	/	/
PCB	Epoxy resin	1.97	26	0.30	/	/

Figure 9 presents the stress contours of the projectile during penetration. As the projectile entered the geometric boundary of the target, the user-defined load function was activated. At the instant of impact (t = 0.025 ms), a stress wave formed at the projectile nose and rapidly propagated toward the tail. The maximum stress magnitude reached approximately 1400 MPa. By t = 0.33 ms, the nose had penetrated into the target. A pronounced stress concentration developed at the front of the inner cavity, reaching approximately 1700 MPa. At t = 1.75 ms, the projectile nose exited the target, and the overall stress dropped. The maximum stress was approximately 1100 MPa.

Table 6 Comparison between the ABAQUS simulation results and the experimental data.

Data type	Simulation	Experiment	Error
Peak deceleration / g	36415	36326	0.25%
Pulse width / ms	1.44	1.32	9.1%
Residual velocity / (m· s^{-1})	641.9	664	3.3%

As shown in Figure 10 and Table 6, the simulated peak acceleration of 36,415 g closely agreed with the experimental value, with a negligible deviation of 0.25%. The pulse width discrepancy between the experimental and numerical results was 9.1%, while the residual velocity error was 3.3%. Meanwhile, by eliminating the need for explicit target modeling, the proposed method significantly improved computational efficiency.

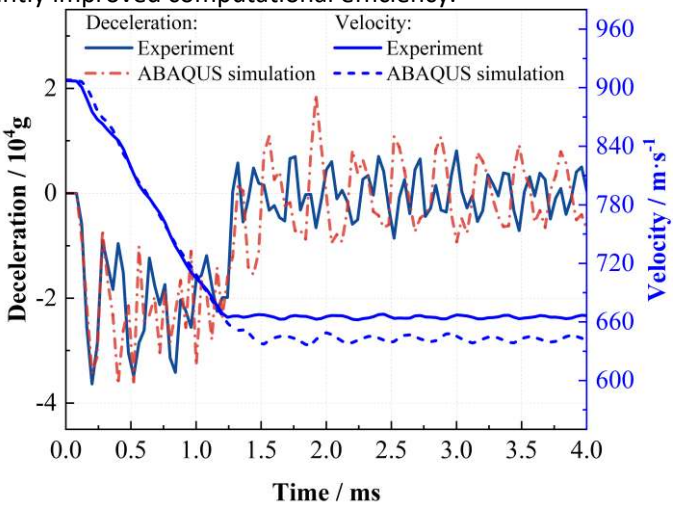


Figure 10 Comparison between the ABAQUS simulation results and the experimental data.

To compensate for the limited experimental data, a 3D finite element model comprising both the projectile and target was developed in LS-DYNA. Leveraging geometric symmetry, a half-symmetry model was adopted to improve computational efficiency, with the symmetry boundary condition enforced via the *BOUNDARY_SPC_SET keyword. Except for the symmetry plane, the target was free of any external constraint. The projectile geometry and material parameters remained consistent with those employed in the ABAQUS model. A graded mesh scheme was applied to the 1-m-thick target plate, and a mesh convergence study was conducted to determine the minimum mesh size of 3 mm in the central impact region. The finite element model is presented in Figure 11, with a total of 7,578,900 elements. The contact between the base plug and the projectile was modeled using *CONTACT_TIED_SURFACE_TO_SURFACE. All other contacts among the projectile components were defined using *CONTACT_AUTOMATIC_SURFACE_TO_SURFACE. The interaction between the projectile and the concrete target was modeled employing *CONTACT_ERODING_SURFACE_TO_SURFACE (Peng et al., 2023; Lin, 2016; Yu, 2022). The concrete target was modeled using the Holmquist-Johnson-Cook (HJC) constitutive model, which incorporates a pressure-dependent strength surface, an equation of state, and a damage evolution criterion. The corresponding material parameters were taken from Guo et al. (2024) and Fang et al. (2015). The HJC model parameters for concrete are listed in Table 7. Meanwhile, the keyword *MAT_ADD_EROSION was activated to control target element deletion, with the maximum principal strain (MXEPS = 0.25) and maximum shear strain (EPSSH = 0.45) specified as failure criteria (Liu et al., 2024).

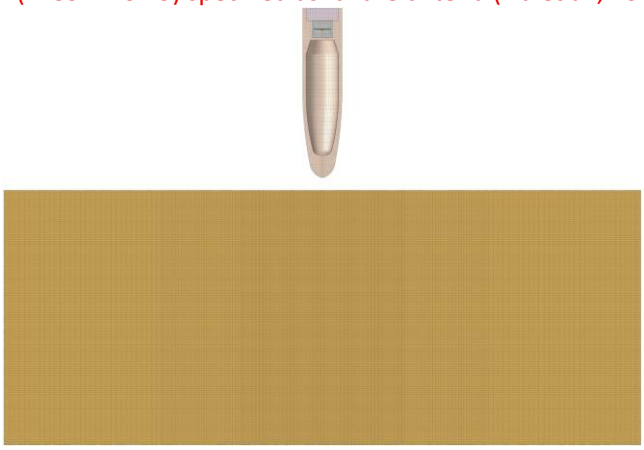


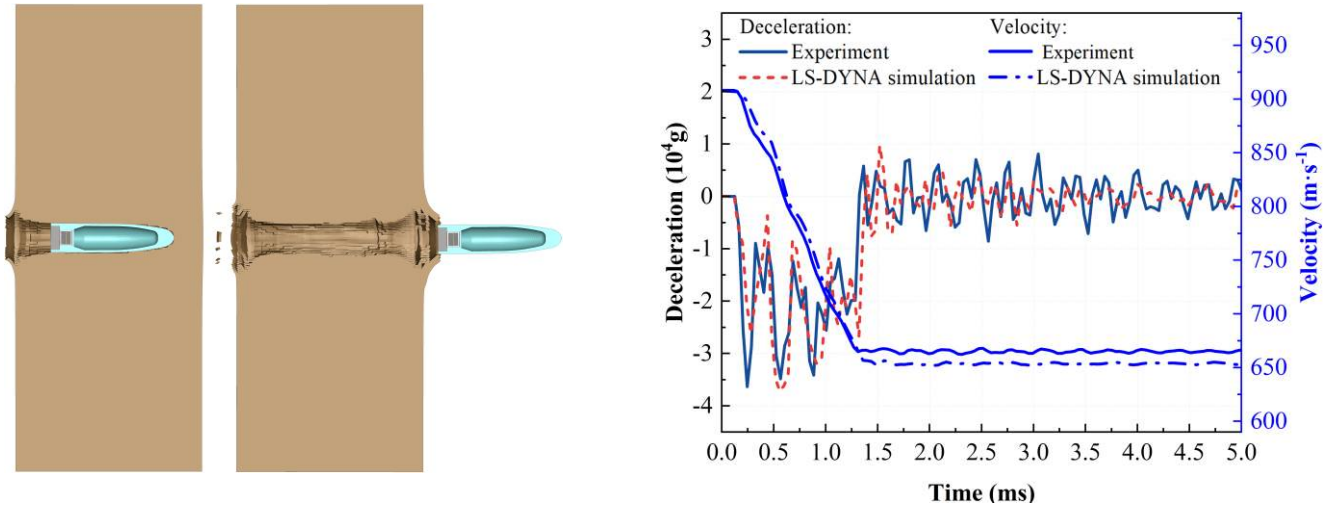
Figure 11 LS-DYNA finite element model.

Figure 12 shows the LS-DYNA simulation results, demonstrating that the developed model well reproduces the cratering and spalling behavior of the target. Figure 12(b) compares the simulated and measured deceleration-time and

residual-velocity curves. The simulated peak deceleration reached 37,175 g, with a relative error of 2.3% compared with the experimental data. The pulse duration was 1.4 ms and the residual velocity was 653 m/s, yielding relative errors of 6.1% and 1.7%, respectively. These comparisons confirmed the reliability of the numerical model. Owing to the difference in the treatment of projectile-target interfacial interaction resistance between the LS-DYNA simulation and the theoretical model in this work, the LS-DYNA model was then applied to compute the dynamic responses of the projectile and its internal electronics under different impact conditions. The results served as benchmarks for both the efficient ABAQUS simulation and the theoretical model.

Table 7 The HJC model parameters for concrete (Guo et al., 2024; Fang et al., 2015).

Parameter	Value	Parameter	Value	Parameter	Value	Parameter	Value
ρ_t / g·cm^{-3}	2.40	C	0.007	EPS0	1×10^{-6}	D_1	0.01
G / GPa	12.98	f_c / MPa	39.2	p_c / MPa	13.7	D_2	1
A	0.79	T / MPa	4.5	p_l / GPa	1.05	K_1 / GPa	85
B	1.60	EFMIN	0.01	u_c	0.00086	K_2 / GPa	-171
N	0.61	SFMAX	7	u_l	0.1	K_3 / GPa	208



(a) (b)

Figure 12 LS-DYNA simulation results: (a) target damage; (b) comparison of the simulated deceleration and residual-velocity histories with experimental data.

For the 908 m/s impact case, all simulations were performed on the same workstation, configured with an Intel Xeon Platinum 8468 processor (48 cores, 2.1 GHz), 256 GB of RAM, and Windows 11 Pro 23H2 64-bit. The software versions used were MATLAB R2020b, ABAQUS 2022, and Ansys LS-DYNA 2022 R1. The wall-clock time and CPU time for this case are summarized in Table 8. The theoretical model required only 0.014 core-hours, whereas the proposed ABAQUS method required 5.33 core-hours. The computational cost of the proposed ABAQUS method was only about 1.35% of that of the LS-DYNA simulation (394 core-hours), which corresponds to a speedup of approximately 74×. This demonstrates that the proposed ABAQUS method is substantially more computationally efficient than the LS-DYNA simulation.

Table 8 Comparison of computational costs among the three approaches.

Method	Software	Cores	Wall-clock time	CPU time / (core-hours)
Theoretical model	MATLAB R2020b	1	52 seconds	0.014
Proposed ABAQUS method	ABAQUS 2022	10	32 minutes	5.33
LS-DYNA full model	Ansys LS-DYNA 2022 R1	10	39.4 hours	394

4.1 Effect of impact velocity on the overload

Figures 13 and 14 compare the deceleration time histories obtained from the theoretical model, the proposed ABAQUS simulation method, and the LS-DYNA full-model simulation at 600 m/s and 1000 m/s, respectively. The agreement between each approach and the full-model simulation was quantified using the Pearson correlation

coefficient r. At 600 m/s, the proposed ABAQUS method achieved a Pearson correlation coefficient of r = 0.95 with the full-model simulation for projectile deceleration, whereas the theoretical model yielded r = 0.93. For the electronic module, the corresponding values were r = 0.71 and r = 0.78, respectively. At 1000 m/s, the ABAQUS simulation achieved r = 0.96 for projectile deceleration, and the theoretical model yielded r = 0.93. The coefficients for the electronic module were r = 0.77 and r = 0.76. In terms of peak deceleration, both methods predicted the projectile response with relative errors below 10%, and errors in the predicted electronic-module response remained below 15%, when compared with the full-model simulation. These results suggested that the proposed ABAQUS method, together with the theoretical model, provided reasonably consistent predictions of the deceleration responses of the projectile and the electronic module, as compared with the LS-DYNA full-model simulations.

Based on the aforementioned ABAQUS method and theoretical model, a parametric analysis was carried out at impact velocities of 600, 700, 800, and 1000 m/s to investigate their influence on the dynamic response. According to Eq. (1), the initial impact velocity primarily governs the dynamic term in the resistance force. Figure 15 illustrates how the peak decelerations vary with velocity. At 600 m/s, the theoretical model yielded peak decelerations of 19,862 g for the projectile and 25,342 g for the electronic module, corresponding to an amplification factor of approximately 1.28. At 1000 m/s, the corresponding values were 27,722 g and 42,740 g, respectively. The amplification factor exhibited an increasing trend with initial velocity.

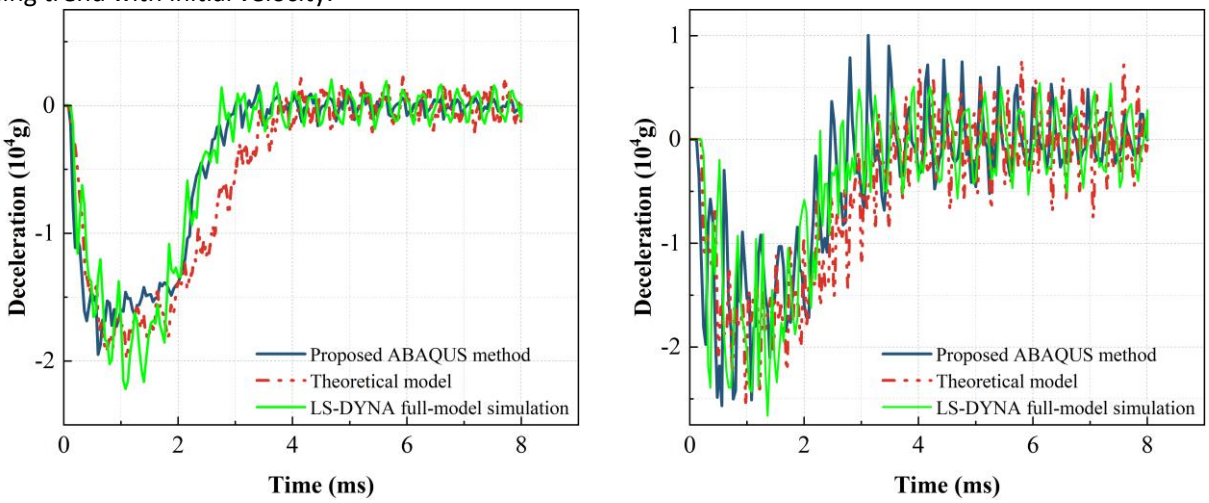


Figure 13 Deceleration–time histories at 600 m/s: (a) projectile, and (b) electronic module.

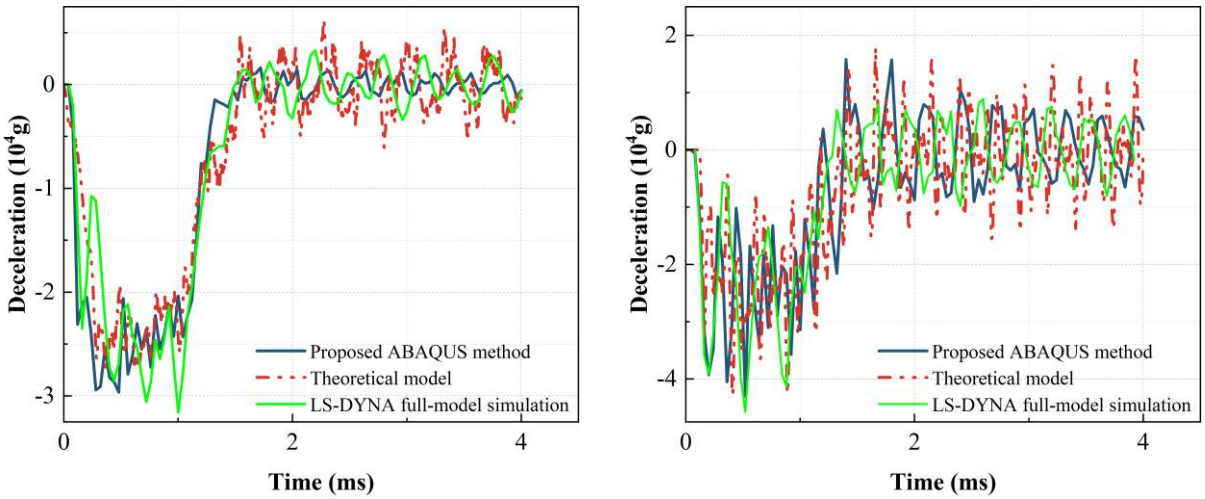


Figure 14 Deceleration–time histories at 1000 m/s: (a) projectile, and (b) electronic module.

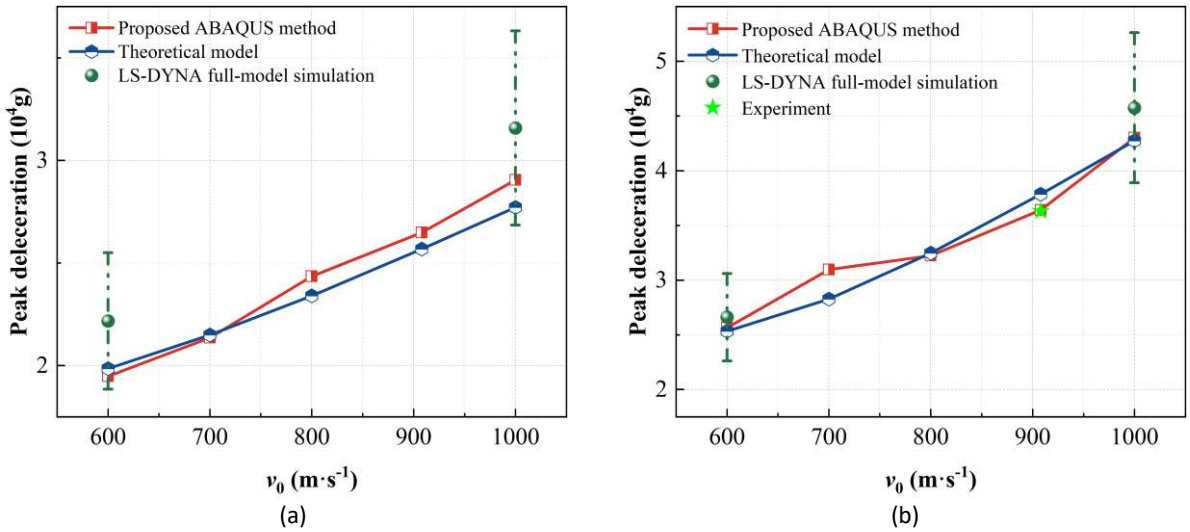


Figure 15 Peak decelerations at different impact velocities: (a) projectile and (b) electronic module.

4.2 Effect of the caliber-radius-head (CRH) of the projectile on the overload

To investigate the influence of projectile nose geometry on the dynamic responses of the internal components, numerical simulations were carried out using projectiles with different caliber-radius-head (CRH) ratios. Based on the baseline projectile described in Section 3.1.1, the nose geometry was changed while the tail structure was retained. Since the projectile contains an internal cavity, directly varying the CRH would result in excessively thin walls in some regions. Therefore, the nose length was slightly increased prior to varying the CRH. The CRH ratio was varied from 1 to 5 with an increment of 1, corresponding to nose shapes ranging from blunt to sharp. Consequently, all five projectiles in this parametric study had a length of 765 mm and a mass of 60.5 kg. The target configuration remained identical to that used in the experiments, and the initial impact velocity was set to 1000 m/s. Figure 16 illustrates the projectile geometries with CRH values of 1, 3, and 5.

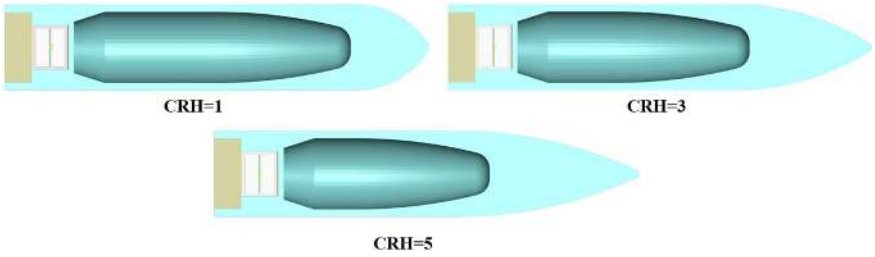


Figure 16 Projectiles with different CRH ratios.

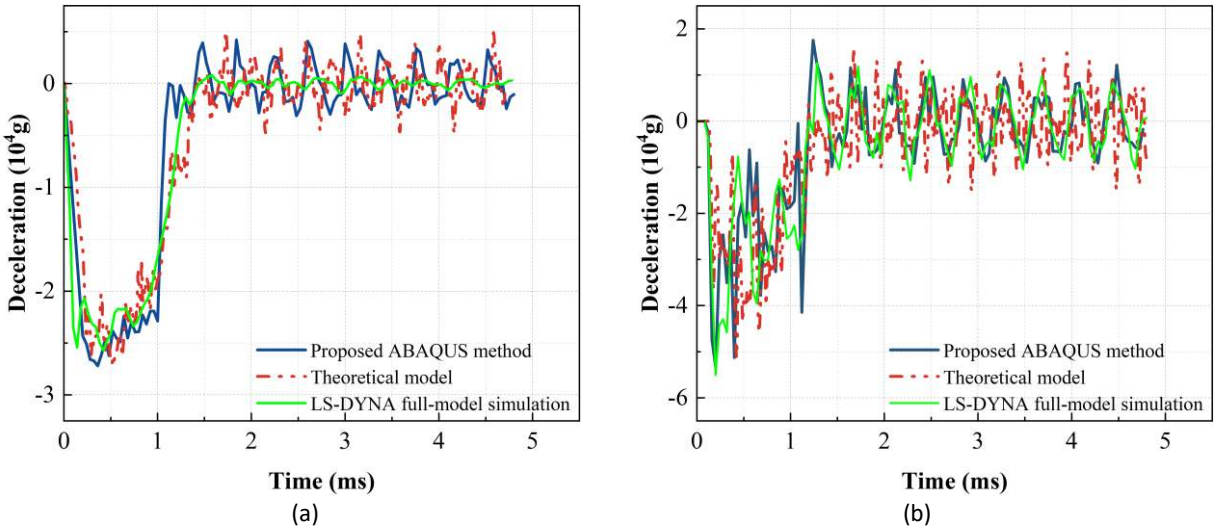


Figure 17 Deceleration–time histories at CRH=1: (a) projectile and (b) electronic module.

Figure 17 compares the deceleration–time histories obtained from the theoretical model, the proposed ABAQUS simulation method, and the LS-DYNA simulation for CRH = 1. For the projectile, the proposed ABAQUS method correlated with the full-model simulation at r = 0.96, whereas the theoretical model yielded r = 0.94. For the electronic module, the corresponding correlation coefficients were 0.83 and 0.71, respectively. The peak decelerations of both the projectile and the electronic module predicted by the two methods exhibited deviations below 15% from the LS-DYNA results. These results demonstrated that the proposed methods maintained satisfactory consistency with the full-model simulation under varying projectile nose geometries.

Figure 18 presents the peak decelerations of the projectile and the electronic module obtained from the proposed ABAQUS method and the theoretical model for CRH ratios ranging from 1 to 5. As indicated by Eq. (8), an increase in the CRH ratio alters the normal angle distribution over the nose surface, which in turn reduces the surface integral of the normal stress and consequently the axial resistance. This geometric effect was most pronounced when the CRH increased from 1 to 3, leading to a sharp drop in peak deceleration. The theoretical model predicted a decrease of approximately 12,000 g, from 50,497 g to 38,921 g. When the CRH ratio further increased from 3 to 5, the peak deceleration decreased by only 4,622 g. Therefore, provided that the structural integrity of the projectile nose is maintained, a larger CRH reduces the peak deceleration of the onboard electronic components, indicating a reduction in the dynamic loading on these components.

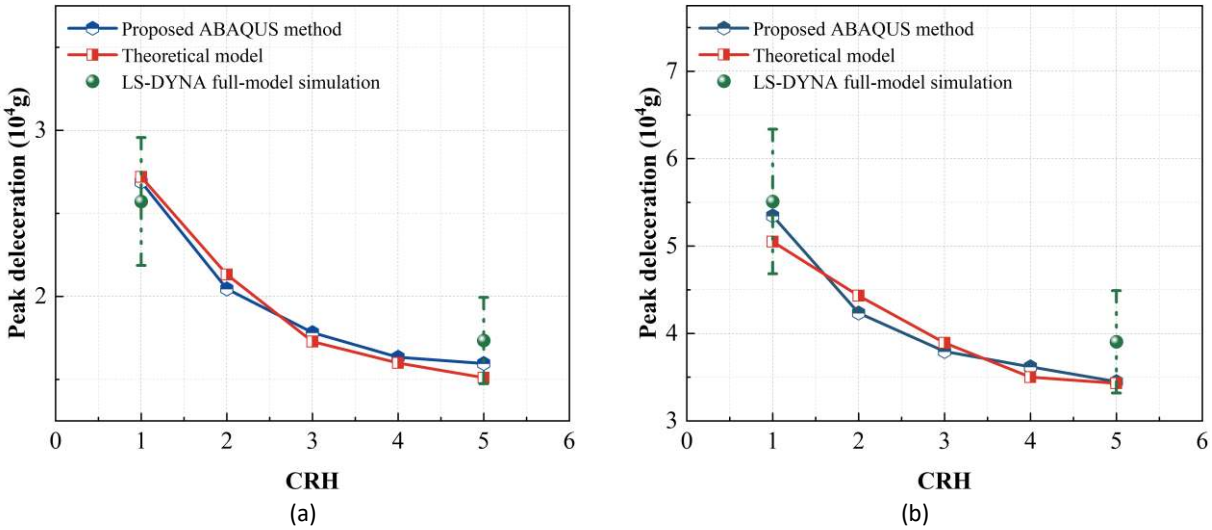


Figure 18 Peak decelerations at different CRH ratios: (a) projectile and (b) electronic module.

4.3 Effect of consecutive impacts on overload

Building on the experimental configuration outlined above, an additional concrete target with the same parameters was introduced to create a second impact zone, with a spacing of 1 m between the two targets. The front and rear surface coordinates of each target define the activation and deactivation of the target resistance. This configuration was devised to explore the dynamic responses of the projectile-borne electronics under consecutive double impacts. The projectile and its electronic module reached peak decelerations of 25,835 g and 36,415 g during the first impact. The projectile exited the first target with a residual velocity of 641.9 m/s. Subsequently, during the second impact, the peak decelerations decreased to 20,277 g for the projectile and 27,907 g for the electronic module.

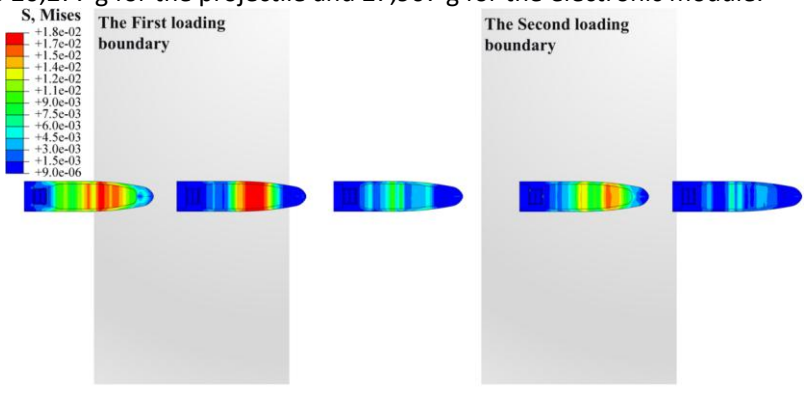


Figure 19 Stress contour of the projectile during consecutive double loading events.

The peak decelerations of the projectile and the electronic module reached 20,436 g and 28,324 g, respectively, when the projectile impacted a single-layer concrete target at a velocity of 641.9 m/s. These values differed from those observed in the second impact. Transient stress waves generated during the first impact contributed to this difference. As shown in Figure 19, multiple reflections and superpositions of these waves inside the projectile gave rise to a highly complex transient vibration state. This transient stress state dynamically modulated the macroscopic deceleration of the projectile during the second impact, leading to changes in the dynamic loading environment of the electronic components.

The time interval between two consecutive impacts was adjusted by varying the spacing of the concrete targets over a range of 0.25 to 5 m. Figure 20 presents the deceleration–time histories obtained from the theoretical model, the proposed ABAQUS simulation method, and the LS-DYNA simulation at a target spacing of 0.25 m. For the projectile, the proposed ABAQUS method correlated with the full-model simulation at r = 0.92, whereas the theoretical model yielded r = 0.89. For the electronic module, the corresponding values were 0.70 and 0.73, respectively. Figure 21 compares the peak decelerations during the second impact predicted by the three methods across various target spacings. Both the proposed ABAQUS simulation method and the theoretical model yielded results within 15% error relative to the LS-DYNA simulation. This consistency demonstrates the applicability of the proposed ABAQUS simulation method and the theoretical model in analyzing the dynamic responses of the projectile and its internal components under consecutive impact loading. Within the spacing range of 0 to 2.25 m, the peak decelerations of the projectile and the electronic module during the second impact did not exhibit a monotonic trend due to the complex stress wave interference from the first impact.

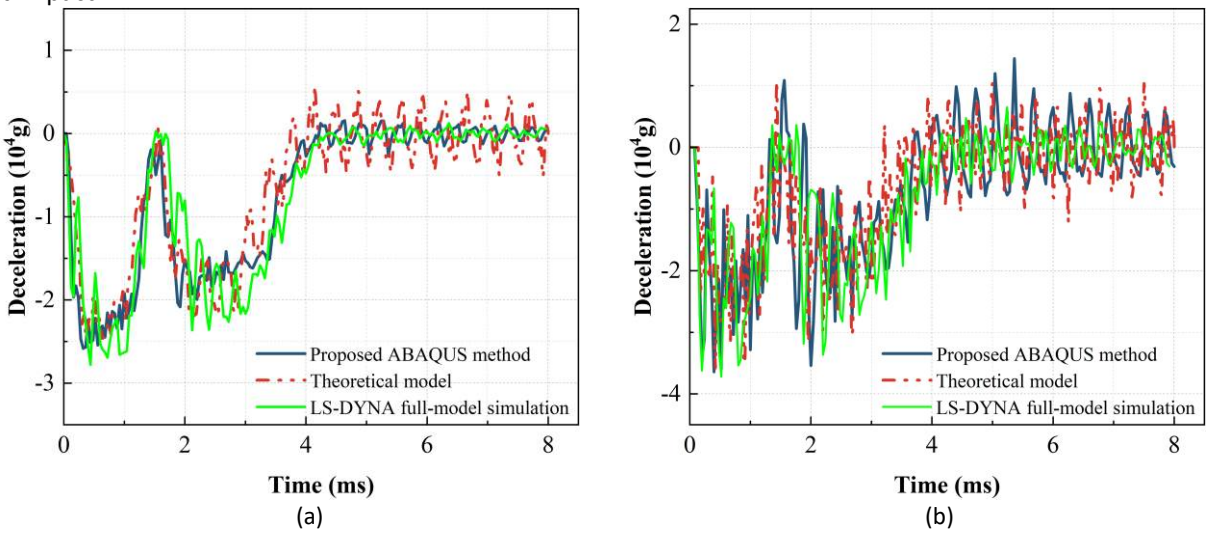


Figure 20 Deceleration–time histories at a spacing of 0.25 m: (a) projectile and (b) electronic module.

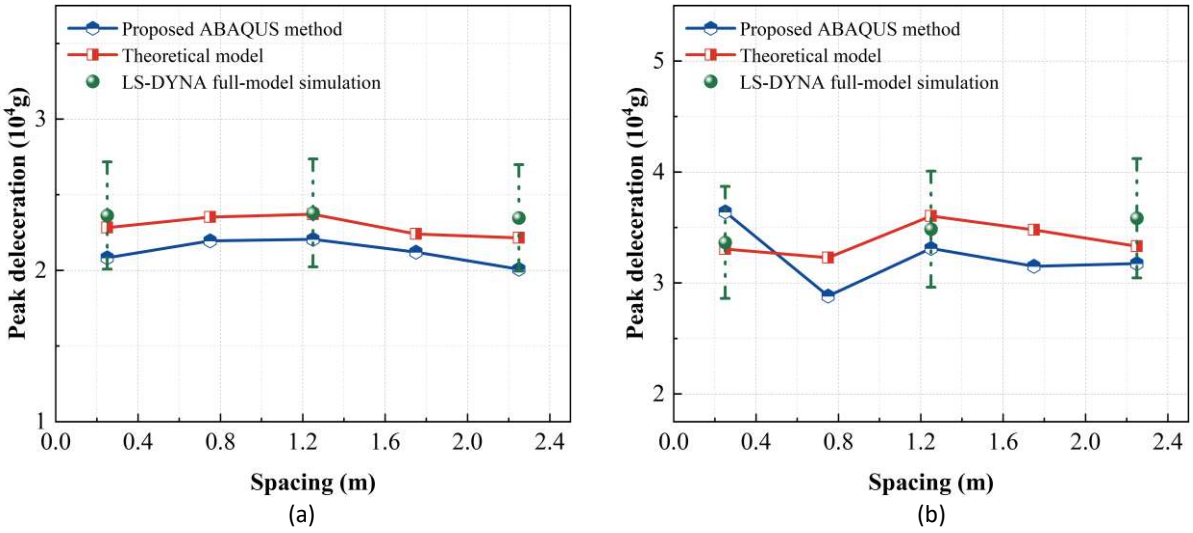


Figure 21 Peak decelerations at different target spacings: (a) projectile and (b) electronic module.

To quantitatively assess the influence of inter-layer spacing on the dynamic response of the electronic module, this study introduces a normalized peak deceleration anorm. An increase in layer spacing extends the interval between impacts, permitting stress waves from the first impact to undergo multiple reflections and dynamic attenuation within the projectile. As a result, the mechanical state of the projectile prior to the second impact more closely approaches its initial stress-free condition. As the inter-layer spacing increased from 0.25 m to 5.0 m, a_{norm} varied non-monotonically and eventually approached 1.0, as depicted in Figure 22. At spacings of 1, 2, 3, 4, and 5 m, the values of a_{norm} were 0.9853, 0.8776, 0.9115, 0.9306, and 0.9936, respectively. All values were below unity, indicating that the first impact still influenced the second impact at these spacings. Eleven out of the fourteen data points lay in the range of 0.9–1.25, and all values for target spacings greater than 4.0 m deviated from unity by within ±7%. These results indicate that when the target spacing is sufficiently large, the influence of the first impact diminishes and a_{norm}converges toward 1.0. However, for smaller spacings, the response is non-monotonic, and increasing the spacing does not consistently reduce the peak deceleration.

$$a_{norm} = a_d / a_s \tag{31}$$

where a_d denotes the peak deceleration during the second impact, and a_s represents the peak deceleration when impacting a single-layer target at the second impact velocity.

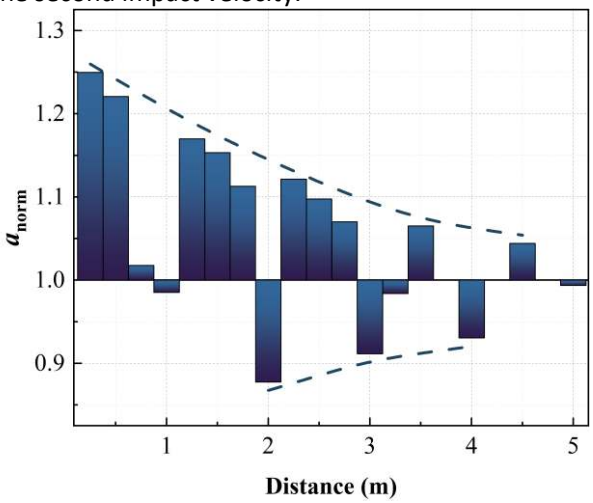


Figure 22 Normalized peak decelerations of the second impacts.

4.4 Applicability and limitations of the proposed simulation method

While the preceding sections have demonstrated the consistency of the proposed ABAQUS simulation method with the LS-DYNA full-model simulations under various conditions, its applicability is subject to inherent limitations. These limitations primarily stem from the physical basis of the theoretical resistance model employed. Figure 23 compares the peak decelerations of the projectile and the electronic module under different target thicknesses, as obtained from the proposed ABAQUS method, the LS-DYNA simulation, and the theoretical model. Substantial discrepancies existed between the results from the proposed method and LS-DYNA simulations at a target thickness of 0.2 m.

The discrepancies observed under thin-target conditions originate from the inherent physical limitations of the analytical surface-loading formulation adopted in this study. Because the concrete target is not explicitly modeled in the proposed method, the accuracy of the structural response depends on the theoretical resistance input. Cavity expansion theory is based on the semi-infinite medium assumption and is applicable to compression-dominated penetration processes into thick targets. For thin-target perforation, target resistance is governed primarily by shear and tensile strengths, representing a fundamentally distinct resistance behaviour compared with that for thick targets. Although the free-surface effect function (Eq. (7)) is introduced in this study to phenomenologically capture resistance reduction induced by target failure modes including shear plugging and rear-face spalling, it provides only a semi-empirical attenuation function for penetration resistance and cannot faithfully reproduce the complex physical mechanisms governing thin-target impact. This is the primary source of the discrepancies.

The free-surface attenuation function $f(d_t, a, \dot{a})$ given in Eq. (7) ranges from 0 to 1 (Kong et al., 2014), where d_t is defined as the sum of the distance from the outward normal of the differential segment to the free surface and the cavity radius a. A smaller d_t corresponds to a more pronounced free-surface effect. For thick targets, the projectile reaches its

peak deceleration before the free-surface effect substantially influences the penetration process. This accounts for the gradual stabilization of peak decelerations of the projectile and the electronic module in Figure 22 with increasing target thickness. For target thicknesses ranging from 0.5 to 1.5 m, the relative errors between the proposed ABAQUS method and LS-DYNA simulations were within 11%, indicating that the approach maintains satisfactory predictive accuracy for engineering applications involving thick targets. Equivalent-load methods of this type have been extensively validated for predicting ballistic trajectories, residual velocities, and dynamic structural responses (Fang et al., 2014; Chen et al., 2018; Xiao et al., 2024; Liu et al., 2025; Shen et al., 2025).

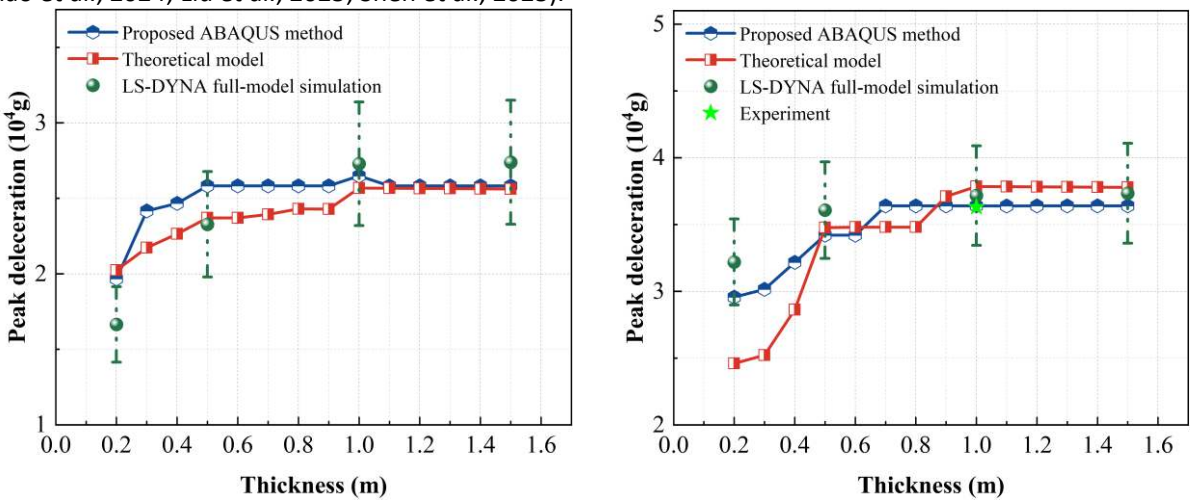


Figure 23 Peak decelerations at different target thicknesses: (a) projectile, and (b) electronic module.

Furthermore, the projectile–target interaction is represented by a user-defined load subroutine applied directly to the projectile surface. When a failure criterion with element deletion is enabled, surface elements are removed upon material failure. This instantaneously removes the load-application boundary, which introduces errors in the load subroutine and may result in computation termination. Therefore, while the proposed method provides high accuracy and efficiency in evaluating the shock responses of the projectile and its internal components, it is not currently applicable to extreme scenarios involving severe fracture or fragmentation of the projectile.

5 CONCLUSION

This study presents a theoretical model and an efficient ABAQUS/Explicit simulation method for predicting the shock responses of projectile-borne electronics under penetration-induced loading. The proposed methods were assessed using a single ballistic impact test and cross-compared with LS-DYNA full-model simulations. The main conclusions are as follows:

(i) The theoretical model predicted the dynamic responses of the onboard electronics with peak deceleration and pulse-width errors of 4.2% and 15.2% relative to experimental data. Furthermore, both the theoretical model and the proposed ABAQUS method showed satisfactory consistency with LS-DYNA simulations under various impact conditions, achieving Pearson correlation coefficients of 0.89–0.96 for projectile responses and 0.70–0.83 for electronic modules, with peak deceleration deviations generally below 15%.

(ii) Impact velocity and projectile nose geometry exert significant effects on the deceleration of the onboard electronics. A marked drop of approximately 12,000 g in the peak deceleration of the electronic module was observed as CRH increased from 1 to 3. Therefore, optimizing the projectile nose geometry provides an effective means of reducing the peak deceleration of onboard electronic devices during penetration. Under consecutive double-impact loading, the dynamic response during the second impact is influenced by the first impact. When the inter-impact interval is sufficiently long, the influence of the first impact on the dynamic response of the electronic module during the second impact diminishes.

(iii) Future experimental investigations are needed to assess the model's applicability across a broader range of penetration conditions. Both the theoretical model and the proposed ABAQUS simulation method have well-defined applicability ranges, and their predictive performance depends primarily upon the adopted equivalent target resistance function. Comparisons with the single test result and LS-DYNA simulation data revealed good agreement for thick-target

penetration, whereas noticeable deviations were observed for thin-target perforation. In addition, the current load-subroutine framework is inapplicable to extreme scenarios involving projectile fracture or severe element erosion.

Author's Contribuitions: Conceptualization, Qiang Sheng; Formal analysis, Qiang Sheng, Xiaoye Bie; Investigation, Qiang Sheng, Xiaoye Bie; Validation, Qiang Sheng; Visualization, Xiaoye Bie; Project administration, Changsheng Li, He Zhang; Funding acquisition, Changsheng Li; Supervision, Changsheng Li; Writing – original draft, Qiang Sheng; Writing – review & editing, Changsheng Li, He Zhang.

Data Availability: Research data is only available upon request.

Editor: Marcilio Alves.

References

Cao Z., Li T., Jing R., et al. (2026). Response characteristics analysis and theoretical prediction model of ultrahigh overload in penetration. Theoretical and Applied Mechanics Letters, 16(1):100696.

Mercurio S.R., Iskander M., Bless S., et al. (2025). Deceleration of projectiles in sand. Acta Geotechnica, 20(2):519-541.

Feng J., Song M., Sun W., et al. (2018). Thick plain concrete targets subjected to high speed penetration of 30CrMnSiNi2A steel projectiles: tests and analyses. International Journal of Impact Engineering, 122:305-317.

Glößner C., Moser S., Külls R., et al. (2017). Instrumented projectile penetration testing of granular materials. Experimental Mechanics, 57(2):261-272.

Verberne P., Meguid S.A., Elsayed E.A. (2021). Survivability of embedded microelectronics in precision guided projectiles: modeling and characterization. International Journal of Impact Engineering, 154:103864.

Fu H., Gao S., Jin L., et al. (2022). Research on the acceleration phenomenon of projectile leaving the target when penetrating thick concrete target. International Journal of Impact Engineering, 164:104191.

Warren T.L., Forrestal M.J., Randles P.W. (2014). Evaluation of large amplitude deceleration data from projectile penetration into concrete targets. Experimental Mechanics, 54(2):241-253.

Booker P.M., Cargile J.D., Kistler B.L., et al. (2009). Investigation on the response of segmented concrete targets to projectile impacts. International Journal of Impact Engineering, 36(7):926-939.

Wu H., Fang Q., Peng Y., et al. (2015). Hard projectile perforation on the monolithic and segmented RC panels with a rear steel liner. International Journal of Impact Engineering, 76:232-250.

Peng Y., Wu H., Fang Q., et al. (2019). Deceleration time of projectile penetration/perforation into a concrete target: Experiment and discussions. Advances in Structural Engineering, 22(1):112-125.

Chen X., Li J. (2014). Analysis on the resistive force in penetration of a rigid projectile. Defence Technology, 10(3):285-293.

Ben-Dor G., Dubinsky A., Elperin T. (2007). Modification of the method of local variations for shape optimization of penetrating impactors using the localized impactor/shield interaction models. Mechanics Based Design of Structures and Machines, 35(1):1-14.

Guo C., Qian J., Gu W., et al. (2023). Penetration characteristics of a penetrator with triangular cross-section impacting semi-infinite targets. Mechanics Based Design of Structures and Machines, 51(3):1335-1348.

Yankelevsky D.Z. (2017). Resistance of a concrete target to penetration of a rigid projectile-revisited. International Journal of Impact Engineering, 106:30-43.

Esaker M., Thermou G.E., Neves L. (2023). Impact resistance of concrete and fibre-reinforced concrete: A review. International Journal of Impact Engineering, 180:104722.

Yang W., Liu Q., Li T., et al. (2026). Establishment of the damage tolerance criterion of projectile-borne electronics in the high-g extreme environment. Theoretical and Applied Mechanics Letters, 16(1):100653.

Chakka V., Trabia M.B., O'Toole B., et al. (2008). Modeling and reduction of shocks on electronic components within a projectile. International Journal of Impact Engineering, 35(11):1326-1338.

Zhang H., Niu S. (2023). Analysis the influence of projectile penetration velocity and length-diameter ratio on fuze overload signal adhesion. Journal of Physics: Conference Series, 2478(7):072035.

Zhang D.M., Gao S.Q., Niu S.H., et al. (2017). Study on collision of threaded connection during impact. International Journal of Impact Engineering, 106:133-145.

Zhang D., Gao S., Xu X. (2016). A new computational method for threaded connection stiffness. Advances in Mechanical Engineering, 8(12):1687814016682653.

Yan A., Wang X., Yang H., et al. (2021). Research on the shock response characteristics of a threaded connection using the thin-layer element method. Applied Sciences, 11(12):5611.

Cheng X., Liu B., Zhao H., et al. (2020). Dynamic modeling and simulation for penetration warhead-fuze system. Acta Armamentarii, 41(4):625.

Yu D., Yang B., Yan K., et al. (2023). Dynamic transfer model and applications of a penetrating projectile-fuze multibody system. International Journal of Mechanical System Dynamics, 3(4):360-372.

Warren T.L., Forquin P. (2016). Penetration of common ordinary strength water saturated concrete targets by rigid ogive-nosed steel projectiles. International Journal of Impact Engineering, 90:37-45.

Warren T.L., Hanchak S.J., Poormon K.L. (2004). Penetration of limestone targets by ogive-nosed VAR 4340 steel projectiles at oblique angles: experiments and simulations. International Journal of Impact Engineering, 30(10):1307-1331.

Zhang D, Gao S. (2022). Vibration characteristics of the threaded connection between a projectile and a fuze during penetration. Explosion and Shock Waves, 42(3): 033302-1-033302-12.

Lu S., Hua D., Li Y., et al. (2019). Stiffness calculation model of thread connection considering friction factors. Mathematical Problems in Engineering, 2019(1):8424283.

Khajehsaeid H., Arghavani J., Naghdabadi R. (2013). A hyperelastic constitutive model for rubber-like materials. European Journal of Mechanics - A/Solids, 38:144-151.

Mooney M. (1940). A theory of large elastic deformation. Journal of Applied Physics, 11(9):582-592.

Machiraju C., Phan A.V., Pearsall A.W., et al. (2006). Viscoelastic studies of human subscapularis tendon: Relaxation test and a Wiechert model. Computer Methods and Programs in Biomedicine, 83(1):29-33.

Chen D., Wu H., Wei J.S., et al. (2022). Nonlinear visco-hyperelastic tensile constitutive model of spray polyurea within wide strain-rate range. International Journal of Impact Engineering, 163:104184.

Jeong K.Y., Cheon S.S., Munshi M.B. (2012). A constitutive model for polyurethane foam with strain rate sensitivity. Journal of Mechanical Science and Technology, 26(7):2033-2038.

Liu C., Sheng Q., Zhang X., et al.(2025) Dynamic response of elliptical cross-section projectiles during penetration into concrete targets with high velocity. Structural Concrete.

Zhu C., Liu C., Sheng Q., Deng Y., Wang X. (2025). Dynamic response of projectile and charge during penetration into concrete target with high velocity. Latin American Journal of Solids and Structures, 22(6):e8546.

Zhu X., Chen X., Zhou H., Zhang H. (2024). Protective performance of gradient encapsulating materials for printed circuit boards in fuze system during impact process. European Journal of Mechanics - A/Solids, 107: 105399.

Yang W., Liu Q., Li T., Han X. (2026). Establishment of the damage tolerance criterion of projectile-borne electronics in the high-g extreme environment. Theoretical and Applied Mechanics Letters, 16(3): 100653.

Yan A., Pi A., Yang H., et al. (2022). Study on the Equivalence of Penetration Overloading for Projectile-Borne Components in Nonproportional Penetrators. Shock and Vibration, 2022(1): 5533064.

Peng J.W., Li C.S., Zhang Y.Z. (2023). Influence of different protective gaskets on Fuze cushioning performance in the process of penetration. Proc. SPIE 12645, International Conference on Computer, Artificial Intelligence, and Control Engineering , 126454T.

Lin S L. (2016). Experiment and Simulation of Projectile Penetrating Concrete Target. Beijing: Beijing Institute of Technology.

Yu D. (2022). Study on high impact dynamic transfer of multi-body system and failure mechanism of typical energy storage devices. Nanjing: Nanjing University of Science and Technology.

Guo T, Sun Y, Luo J, et al. (2024). Numerical Calculation and Analysis of Anti-penetration of Ultra-high Strength Bullet Shielding Layer. Journal of Physics: Conference Series, 2891(4): 042023.

Fang Q, Luo M, Zhang J H, Sun Z Y. (2015). Numerical analysis of the projectile penetration into the target of corundum-rubble concrete composite overlay. Explosion and Shock Waves, 35(4): 489–495.

Liu B, Guo R, Kang Y, et al. (2024). Numerical Simulation of Rigid Projectile Penetrating Concrete and Granite. Journal of Xiangtan University (Natural Science Edition), 46(4): 28-39.

Kong X, Fang Q, Wu H. (2014). Terminal Ballistics Study of Deformable Projectile Penetrating Brittle Material Targets for Free-surface andCrack Region Effects. Acta Armamentarii, 35(6): 814.

Fang Q., Kong X., Hong J., Wu H. (2014). Prediction of projectile penetration and perforation by finite cavity expansion method with the free-surface effect. Acta Mechanica Solida Sinica, 27(6): 597-611.

Chen X., Lu F., Zhang D. (2018). Penetration trajectory of concrete targets by ogived steel projectiles–Experiments and simulations. International Journal of Impact Engineering, 120: 202-213.

Xiao X, Feng S, Gao Y, et al.(2024) Trajectory prediction of rigid projectile for oblique penetration into multi-layer aluminum targets. International Journal of Impact Engineering, 190: 104967.

Shen T, Liu C, Li P, et al.(2025) Analysis of Deflection Law of Elliptical Cross-sectional Projectiles Penetrating into Thin Concrete Targets. Acta Armamentarii, 46(12): 250477-1.